# Anisotropic electrospun honeycomb polycaprolactone scaffolds: Elaboration, morphological and mechanical properties

Hugues Mondésert, Frédéric Bossard, Denis Favier

# Anisotropic electrospun honeycomb Polycaprolactone scaffolds: elaboration, morphological and mechanical properties

*Hugues Mondésert* [a, b], *Frédéric Bossard* [a], *Denis Favier* [b]

[a] Univ. Grenoble Alpes, CNRS, Grenoble INP*, LRP, 38000 Grenoble, France

[b] Univ. Grenoble Alpes, CNRS, Grenoble INP*, TIMC-IMAG, F-38000 Grenoble, France

* *Institute of Engineering Univ. Grenoble Alpes*

## Abstract

Tissue engineering technology requires porous scaffolds, based on biomaterials, which have to mimic as closely as possible the morphological and anisotropic mechanical properties of the native tissue to substitute. Anisotropic fibrous scaffolds fabricated by template-assisted electrospinning are investigated in this study. Fibers of electrospun Polycaprolactone (PCL) were successfully arranged spatially into honeycomb structures by using well-shaped 3D micro-architected metal collectors. Fibrous scaffolds present 2x4 mm² wide elementary patterns with low and high fiber density areas. Distinct regions of the honeycomb patterns were analyzed through SEM images revealing different fiber diameters with specific fiber orientation depending on the regions of interest. Tensile test experiments were carried out with an optical observation of the local deformation at the pattern scale, allowing the determination and analysis, at small and large deformation, of the axial and transverse local strains. The honeycomb patterned mats showed significantly different mechanical properties along the two orthogonal directions probing an anisotropic ratio of 4.2. Stress relaxation test was performed on scaffolds at 15% of strain. This measurement pointed out the low contribution of the viscosity of about 20% in the mechanical response of the scaffold. An orthotropic linear elastic model was consequently proposed to characterize the anisotropic behavior of the produced patterned membranes. This new versatile method to produce architected porous materials, adjustable to several polymers and structures, will provide appealing benefits for soft regenerative medicine application and the development of custom-made scaffolds.

KEYWORDS: Mechanical Anisotropy/ Scaffolds / Electrospinning / Honeycomb patterns

HIGHLIGHTS:

- Microstructured collectors were designed to collect and organize electrospun fibers
- Fibrous scaffolds with repetitive honeycomb patterns were successfully fabricated
- Structured membranes exhibit an anisotropic mechanical behavior similar to natural tissues
- This method provides a novel strategy to design anisotropic scaffolds for soft tissue regeneration

# 1. Introduction

Natural tissues in the human body exhibit various morphologies and complex architectural structures depending on the function they fulfill within the living organism (Engelmayr et al., 2008; Fung, 1995). The Extra-Cellular Matrix (ECM) is formed of an intricate meshwork of pores, fibers and bridges based on collagen fibrils and elastin bundles (Flemming et al., 1999; Ní Annaidh et al., 2012). Such natural frameworks are anisotropic and spatially organized to provide a mechanical support and to favor cell adhesion, colonization and proliferation. Biomimetic scaffolds consequently require similar anisotropic architectures to mimic in the best way the structural function of the injured tissue (Ma, 2008). Previous studies have shown the relevance of membrane topography for cell activity. Cell alignment, proliferation and functional performance are triggered by structural features of scaffolds (Tallawi et al., 2016; Criscenti et al., 2017; Kuppan et al., 2017; Kang et al., 2018), suggesting that anisotropy is a key component for a healthy tissue development.

Electrospinning has been used over the last decades as an efficient elaboration technique to produce tridimensional scaffolds for regenerative medicine. Indeed, this simple and versatile process allows the fabrication of polymer networks based on fibers with micro or nano-scales diameters, forming a mat with a thickness of few hundred of microns to centimeters. Electrospun fibrous mats exhibit attractive structural properties such as high porosity, large surface to volume ratio and good pore interconnectivity that make them suitable candidates for soft tissue engineering scaffolds (O'Brien, 2011). Due to the instability

of the polymer jet during the whipping phase, conventional electrospinning produces non-woven fibrous mats with a random fiber deposition and consequently in plane isotropic properties. Main hypotheses on fiber structuration state that final scaffold morphology is driven by a few factors such as electrostatic forces, remaining charges within the fibers (S. Nedjari et al., 2015), speed and chaotic trajectory of fiber paths induced by the whipping instability, or surface area energy effect (Yao et al., 2019).

Anisotropy was introduced into electrospun membranes by triggering the spatial fiber organization using specific collectors such as rotating mandrels or non-flat and homogenous templates such as grids or wirenets. Early studies succeed to align fibers toward preferential directions using collectors rotating at high velocity (Li and Wang, 2003; Liu and Dzenis, 2008; Beachley, 2011; Zhou and Tan, 2017; Li et al., 2019). This first simple method, widely used to produce aligned fibers, is also known to reduce their diameter due to the rotational force applied by the drum (Alfaro De Prá et al., 2017). Moreover, high rotational speed of the drum disturbs the stability of the jet and often breaks the fiber that could weaken the mechanical properties of the entire scaffold.

Collectors made with two conductive parts separated by an isolative gap can as well be used to form fiber bridges with high alignment (Liu and Dzenis, 2008; Beachley and Wen, 2009; Beachley, 2011; Vaquette and Cooper-White, 2011; Bayati et al., 2013; Dippold et al., 2017; Shah Hosseini et al., 2018). Shah Hosseini et al. (Shah Hosseini et al., 2018) produced aligned PLLA fibers onto 3D static collectors based on a 2-bands gap technique. They obtained with a small tip-to-collector distance and high voltage a controlled fiber orientation. Even if interesting methods have been studied to sustain the alignment of the fibers (Bayati et al., 2013), insulating gap produces unidirectional fibers in a small quantity and over a small distance, making the use as scaffolds difficult. The two previous methods provide a way to align fibers only in one selected direction, giving a restricted flexibility in the design of more complex degree of anisotropy representative of natural tissues.

Other recent researches have shown interesting improvements in patterning fibers using 3D templates. Conductive or non-conductive supports allow the local modification of the electric field at the vicinity of the collector. Fibers follow a specific path driven by the electrostatic forces induced by the electric field and deposit onto the more attractive parts of the collector. Zhang et al. (Daming and Jiang, 2008; Zhang and Chang, 2007) are the first to introduce patterns in their tubular electrospun structures. In their work, collected fibers formed square patterns with an order degree depending on feeding rate, voltage and solvent

composition. Metal wire nets or grids were investigated as conductive collectors in a few publications (Neves et al., 2007; Munir et al., 2008; Vaquette and Cooper-White, 2011; Titov and Tan, 2016; Kang et al., 2018). In these cases, fibers are deposited preferentially on the metal mesh areas and adopt the same macroscopic shape of the collectors. Fibrous mats with repetitive structure can be produced using protrusion collectors (Zhang et al., 2009; Wang et al., 2010; Qiao et al., 2018). Yujie Qiao et al. (Qiao et al., 2018) fabricated polycaprolactone–collagen– silk fibroin electrospun scaffolds by collecting on probe array collectors. Membranes produced onto such 3D templates are thin, hard to remove from their supports and show often a low level of structuration decreasing with collection time.

Scaffolds with honeycomb-like structures have promising properties for cell tissue engineering. They provide an anisotropic structure with a large surface area and zones with low and high porosity which can promote cell development (George et al., 2006; Yao et al., 2019). Yao et al. (Yao et al., 2019) described in their work the elaboration of self-assembled honeycomb structures on flat collectors. Gradient honeycomb patterned meshes with a 100 µm thickness were induced by the opposite actions of surface tension and electrostatic repulsion. Similar structures can be achieved by the fluctuation of fiber diameter in a beads-like morphology or by combining electrospinning and electrospray techniques (Ahirwal et al., 2013; Garcia Garcia et al., 2018; S. Nedjari et al., 2015). Thicker fibers, easily discharged in contact with the collector, would define attractive areas for new incoming fibers whereas smaller overhanging fibers would repulse them inducing a self-assembly organization. In these cases, patterns adopted a hexagonal like configuration that resembles more to a Voronoi tessellation than to a regular honeycomb pattern. More symmetrical honeycomb shaped scaffolds can be produced by template assisted electrospinning. Rogers et al. (Rogers et al., 2014) used patterned resin formers covered by thin gold layer to reproduce reentrant honeycomb structures.

Mechanical properties of isotropic random electrospun fibers are commonly assessed with axial tensile tests (Lee et al., 2003; Katsube et al., 2008; Croisier et al., 2012; Domaschke et al., 2020). Silberstein et al interestingly demonstrated that mechanical properties of random electrospun mats were closely linked to the fiber/fiber interactions. Bending of transverse fibers would influence densification and alignment of fibers and consequently determine mechanical behaviors of the mats such as stiffness and transverse contraction (Silberstein et al., 2012). Similarly, Simonet et al have shown that low

temperature electrospun matrices exhibit higher porosity and void space between fibers that lower globally the mechanical properties of the scaffolds (Simonet et al., 2014).

Only a few of publications discuss about mechanical properties of patterned fibrous membranes made by electrospinning (Kang et al., 2018; Neves et al., 2007; Vaquette and Cooper-White, 2011; Wang et al., 2009; Yan et al., 2013). Basically, the introduction of a fiber organization affects the global mechanical behavior of the electrospun scaffolds. In the case of fiber bundles, mechanical anisotropy can be evaluated by comparing tensile stress in directions along and perpendicular to fiber orientation (Chou and Woodrow, 2017; Jamadi et al., 2016; Wu et al., 2019). Shamsah et al. (Shamsah et al., 2019) investigated the mechanical response of aligned PCL fibers undergoing a loading in the direction of 0, 30 or 60° to fiber directions. They showed that tensile properties are directly connected to the loading direction. The greater the angle is between the load axis and the direction of fiber alignment, the weaker is the cohesion between fibers resulting in reduced mechanical properties. Aligned electrospun scaffolds are rarely characterized mechanically along the transverse direction (90°), without taking into account the important anisotropy of the scaffolds.

Electrospinning is used with a large range of polymers. Among them, Polycaprolactone PCL is a well-known synthetic polymer widely used for biomedical applications. Its bio compatibly and bioresorbability properties, low cost and easy electrospinnability make PCL electrospun fibers attractive materials for tissue engineering (Janmohammadi and Nourbakhsh, 2019).

In this study, a technique with new electro-conductive collectors to create anisotropic scaffolds is described and used to fabricate PCL fibrous mats with a repetitive honeycomb pattern. The aim of this work is to introduce a new anisotropic custom made scaffolds, evaluate their mechanical properties and link them to their structural aspects. Firstly, heterogeneous fibrous membranes are characterized depending on the different areas of the pattern. Then mechanical properties of these new biomaterials are investigated to highlight their anisotropic behaviors, with respect to the local deformation of the pattern. Finally, an orthotropic linear elastic model is introduced to model the mechanical behavior at small strains of the structured scaffolds.

# 2. Material and methods

*2.1 Materials*

Poly(ε-caprolactone) (PCL) with a mean molecular weight of 80 000 g/mol, Dichloromethane (DCM ≥ 99.9 %) and Methanol (MeOH > 99.5 %) were purchased from Sigma Aldrich. All polymer solutions for electrospinning were obtained by dissolving PCL pellets in a two solvents blend (DCM and MeOH) with a volume ratio of 4/1. Solutions were stirred with a roller mixer device for 24 hours minimum at room temperature in order to obtain a clear and homogeneous solution. Polymer solutions within a range of 8 to 16 wt% were investigated in reference to previous works of Lancuski et al. (Lancuški et al., 2013, 2012). A solution at a concentration of 16 wt% providing uniform and bead-free fibers was experimentally selected.

*2.2 Electrospun membranes elaboration*

A vertical electrospinning apparatus was used to produce PCL polymer fibers. Set up consists of a syringe pump (model: KDS Legato 200, KD Scientific, Holliston, MA, USA) containing the polymer solution and a voltage source (±30 kV , iseq GmbH, Radeberg, Germany) as shown in **figure 1.a**. A 5 mL syringe with a 21 Ga metal needle tip was loaded with the polymer solution and a constant flow rate of 5 mL/min was applied. Distance between the tip of the needle and the collector was adjusted at 20 cm and the applied voltage varied from 12 to 20 kV. Fibers were collected for 10 to 15min on their templates at a temperature of 21°C, with a humidity controlled between 40 to 60 %.

Fibers were projected to form wide fibrous membranes onto a patterned collector made of a brass metal cross of 70 mm wide (**figure 1.b**). The so formed micro-structured collectors are composed of small metal peak arrays placed on the top as shown in **figure 1.c**. Protrusions, obtained by electro-erosion, are disposed in a specific honeycomb pattern. Distances $d_0^\circ$, $d_2^\circ$, $d_3^\circ$ and $d_4^\circ$ **(figure 1.d)** are equal to 4 mm, 1.4 mm, 1 mm and 2 mm respectively. Protrusions are 1mm high and have a square base (300 µm large). They were

designed with a pyramidal shape at the top in order to accentuate the local modification of the local electric field.

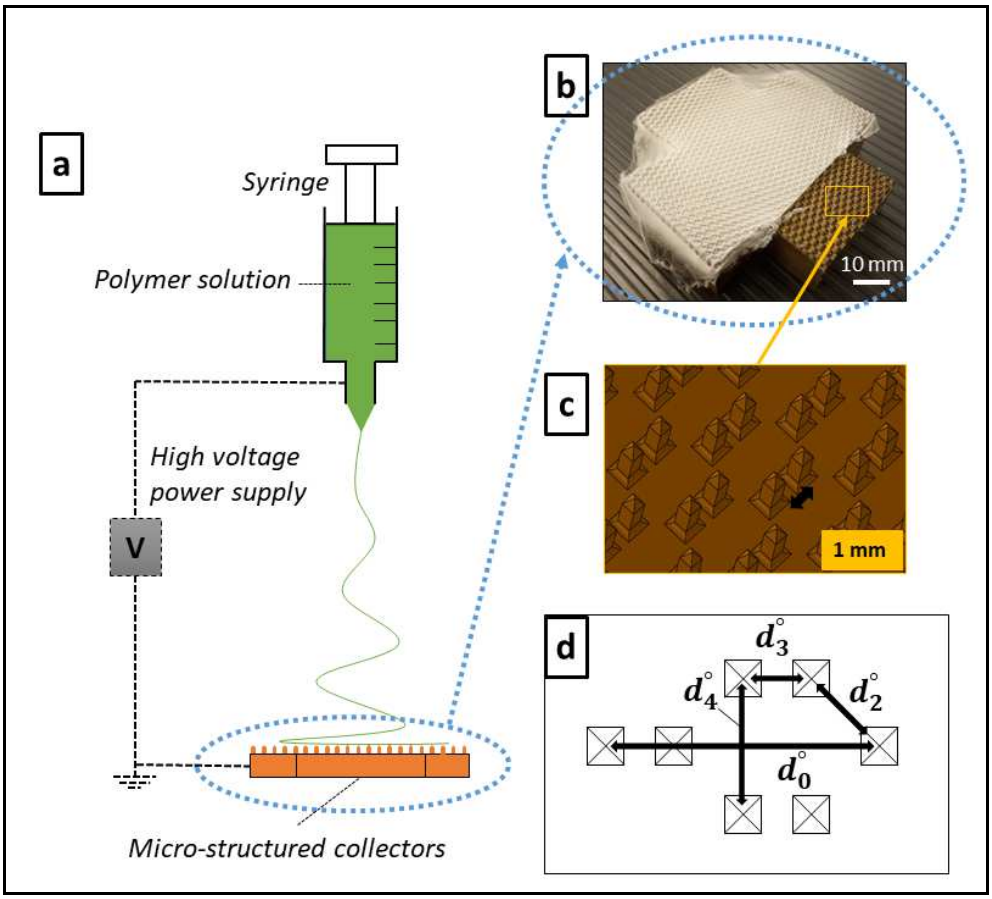


*Figure 1 – Electrospinning set up: a) fiber patterning on microstructured collectors, b) fibrous membrane deposited on microstructured collectors, c) 3D view of microstructured collectors, d) elementary honeycomb mesh (top view of the collector protrusions: distances are $d_0^\circ$ = 4 mm, $d_2^\circ$ = 1.4 mm, $d_3^\circ$ = 1 mm and $d_4^\circ$ = 2 mm)*

### *2.3 Morphological characterization set up*

Optical microscopes (Olympus, Keyence) were used with transmission mode to observe honeycomb micro-structures and assess local arrangement of the fibers. A field-emission–scanning electron microscope (FESEM ZEISS ULTRA55) was used to characterize the structure at the fiber scale. Fibrous samples were previously coated with a thin carbon layer by sputtering for SEM imaging. Measurements over 100 different fibers were made to estimate the average fiber diameter (AFD). Fiber orientation analysis was performed with ImageJ software using the plugin OrientationJ to extract the local 2D orientations of the fibers based on structure tensors (Püspöki et al., 2016). Profilometer scan of the patterned scaffolds

was performed with a numerical microscope, Keyence, VHX-7000, (magnification x50, numerical aperture 0.9, motorized xy plate (1 µm presision).

*2.4 Mechanical characterization set up*

Uniaxial tensile tests were carried out with an ARES-G2 rheometer (TA Instruments, New Castle, DE, USA). Samples were cut in rectangular shapes ($l_0$ = 10 mm, $L_0$ = 70 mm) (see **figure 2.a**) using a sharp blade. Sample extremities were placed into two axial clamps. In order to avoid local damage of the scaffolds induced by the grips, small strips of paper tape were added between the sample and the grip. Samples were stretched along one direction at a constant crosshead speed of 0.1 mm/s. Gauge length $H_0$ was set at 30 mm. ARES-G2 rheometer is equipped with a normal force transducer of 20 N (0.001 N precision) and a positioning accuracy of 0.1 µm. Uniaxial tensile tests were performed at least on three samples in the two perpendicular directions $D_1$ and $D_2$ defined in **figure 2.a**.

The produced membrane exhibit an irregular profile that makes the determination of an accurate thickness delicate. However, this parameter is required to determine the nominal stress $\sigma = \frac{F}{l_0 \langle e \rangle_0}$ of the membrane tensile test, with $F$ the measured axial force, $l_0$ the initial width and $\langle e \rangle_0$ the initial apparent thickness of the sample. It is worth noting that the true stress cannot be used as the thickness of the membrane $\langle e \rangle$ , thus the exact cross section, cannot be evaluated at every step of the tensile deformation.

An alternative method is proposed in this study by measuring sample mass $m$. As shown in the following equation, the reverse porosity $(1 - p)$ can be expressed as:

$$(1 - p) = m \,/\, \rho_{bulk} \, L_0 \, l_0 \, \langle e \rangle_0 \quad (1)$$

where $\rho_{bulk}$ denotes the bulk density of PCL (1.145 g/cm$^3$) , $p$ the porosity and $L_0$ , $l_0$, $\langle e \rangle_0$ the initial dimensions of the fibrous sample. Using the first equation the nominal stress can thus be calculated as:

$$\sigma = \frac{F \, L_0}{m} \rho_{bulk} \, (1 - p) \quad (2)$$

Porosity of all samples was considered constant since electrospinning parameters are identical. It was experimentally measured with a first honeycomb sample by measuring its thickness $\langle e \rangle_0$ and mass $m$ (**equation 1**). Initial thickness $\langle e \rangle_0$ was measured by a mechanical

compression test with a Haake MARS III, Thermo Scientific rheometer (maximum axial force of 0.1 N with a parallel plate geometry (diameter of 20 mm). The obtained value of 94 % was calculated and considered as reference for later analysis.

In this way, we introduce a way to compare patterned samples with a mass measurement which was found experimentally more accurate than measuring apparent thickness $\langle e \rangle_0$ of each sample. This approach is also less intrusive than measuring average thickness since rectangular membranes are non-damaged by a mechanical micrometer prior to tensile tests.

A camera (Basler acA2000-50 gm) was installed on the tensile stress measurement bench. A motorized device enables to follow the center of the gauge length of the sample during elongation and the deformation of a few honeycomb patterns. Patterns situated at the center of the sample are considerably less altered by the presence of the grips, which restrain locally the transverse deformation of the fibrous material. As shown in **figure 6**, membranes adopt from 15% of strain a dog bone shape characteristic of a non homogenous deformation. Stacks of images were processed with imageJ software in order to calculate local axial and transverse strains at the core of the mechanical sample (more details in § 4.2).

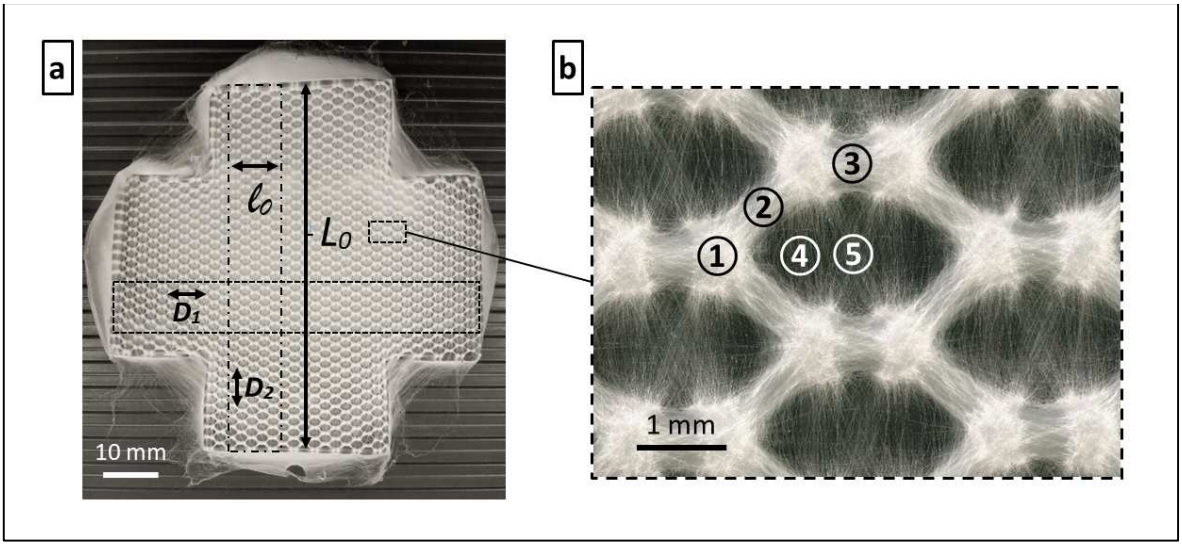


*Figure 2 – a) Electrospun cross membrane from where tensile samples $D_1$ and $D_2$ were extracted ($l_0$=10 mm and $L_0$ = 70 mm), b) Honeycomb patterns of the fibrous scaffold*

# 3. Morphology characterization

*3.1 Description of the honeycomb elementary mesh*

Optical and SEM Images (**figures 2 and 3**) were performed to observe the structure of the fibrous membranes. Fibers (in white) are spatially arranged in honeycomb patterns over the 70 mm-wide metal cross as shown in figure 2.a. The fibrous mats, obtained with high reproducibility, recreate in a very satisfactory way the elementary pattern of the 3D metal support as observed in several template assisted electrospinning processes (Wu et al., 2010; Vaquette and Cooper-White, 2011; Salima Nedjari et al., 2015). 3 zones can be distinguished in **figure 2.b**: a dense area located at the corners of the honeycomb pattern ①, a zone between two protrusions where fibers form bridges ② and ③, and a central area of low density at the core of the pattern ④ and ⑤. Dense areas ①, ② and ③ will confer the required mechanical strength to the global framework whereas low dense zones ④ and ⑤ associated with a lower porosity would provide a favorable environment where cells could penetrate in depth and proliferate. Studies (Soliman et al., 2011; Vaquette and Cooper-White, 2011) demonstrated that electrospun scaffolds with lower fiber density and increased pore size showed a better cell proliferation and infiltration within the scaffolds. Consequently, the presented method brings a new way to build organized heterogeneous materials combining an attractive structural environment for cells with anisotropic compact structures.

Column 1 of **figure 3** shows SEM images focused on each of the honeycomb zones ① to ⑤ defined in **figure 2.b**. The first zone ①, shown in **image 3.1,** is composed of randomly orientated fibers. The brightness of the zone on the SEM images points out that density of fibers is higher at the junction points of the honeycomb, corresponding to the protrusions of the collector. Between protrusions, corresponding to the zones ② and ③, aligned fibers are collected and form bridges (**images 3.2 and 3.3**). Areas ④ and ⑤, in **images 3.4 and 3.5** respectively, displayed a weaker fiber density. Nevertheless, the few fibers are still organized in two directions and clearly shaped a cross in those areas. With these non-flat collectors, the electric field is slightly disturbed, especially at the vicinity of the collector (Titov and Tan, 2016; Zhang et al., 2009). Pyramidal protrusions of the collectors

enhance the electrical point effect. Once fibers are close to the surface of the collector, they are more attracted to protrusions and preferentially accumulated on their tops. Continuous fiber jet will follow a preferential path to connect to close neighbor protrusions. This path depends on the fiber flexibility and the intensity of the local electric field. During the deposition, the probability for a fiber in contact with a protrusion to connect to its neighbor is higher along the fiber direction. The fact that bridges ③ are wider than ② reinforces the deposition mechanism based on the electrostatic attraction. Protrusions represent a more attractive pole, thus the fiber will be steered with higher probability toward its closest neighbor protrusions. Only a few fibers are crossing the gap in the center of the honeycomb mesh which represents a longer distance for the fiber to overcome. A second hypothesis considers the remaining charges accumulated by fibers and the electrostatic repulsion they create. As explained by Wittmer et al. (Wittmer et al., 2014), fibers in the center of the mesh have more difficulty to release the positive charges compared to the fibers situated on the protrusions. Additional electrostatic repulsion forces will appear and guide new approaching fibers, resulting in a structuration.

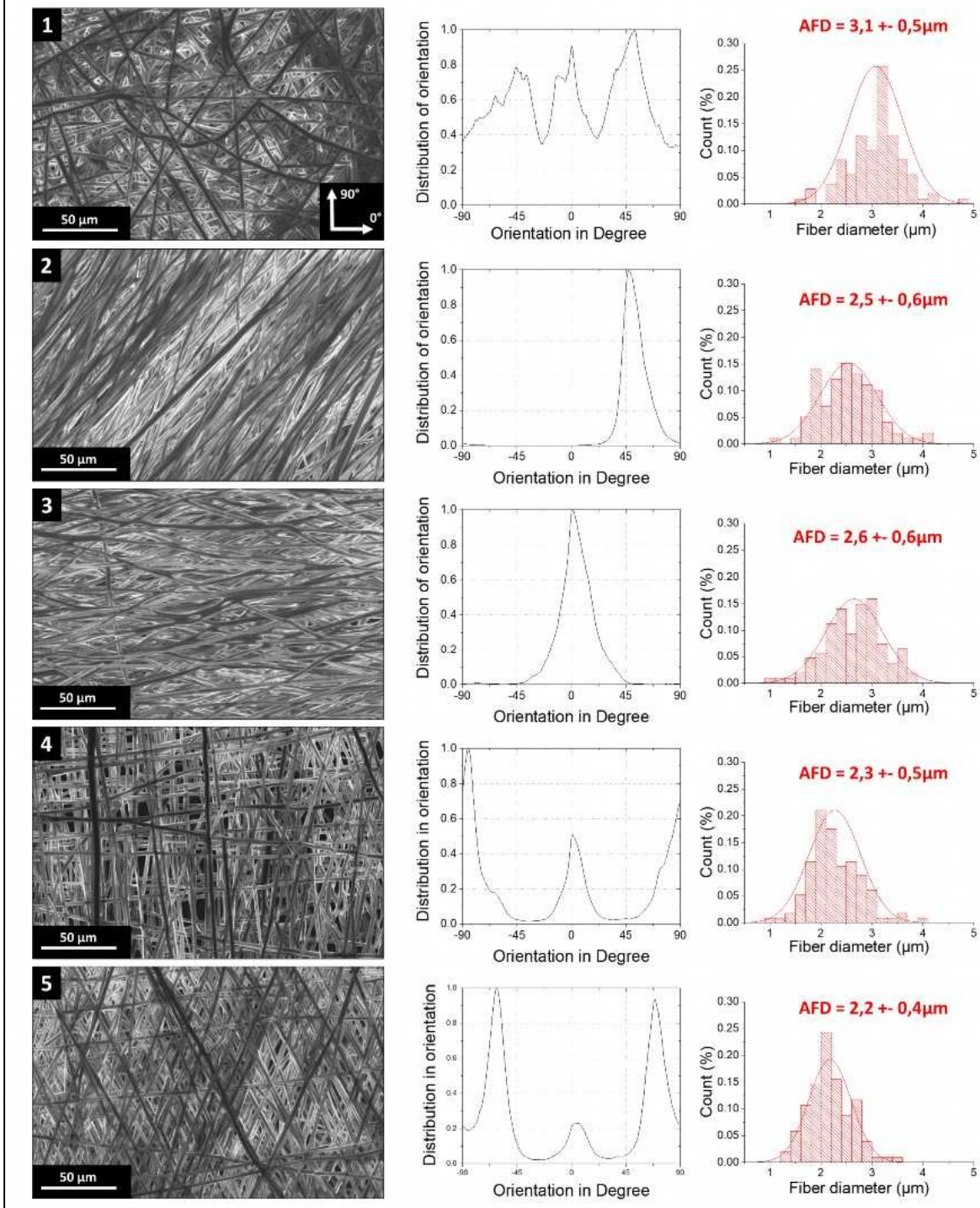


*Figure 3 - SEM images of honeycomb scaffolds with fiber orientation and Average Fiber Diameter measurements: ① high fiber density zone (collector protrusions), ② and ③ fiber bridges, ④ and ⑤ center of the honeycomb pattern*

*3.2 Orientation and fiber morphology*

Column 2 of **figure 3** shows the fiber orientation distribution in the areas ① to ⑤ of the honeycomb mesh. It is clear that fibers align preferentially along a unique direction for the bridges ② and ③ with a characterized orientation of 45 ° (**figure 3.2**) and 0 ° (**figure 3.3**) respectively. These preferred orientations correspond precisely to those of two neighbor protrusions in this part of the elementary cell and likely due to a local modification of the electric field in the vicinity of two protrusions. **Figure 3.1**, corresponding to the zone ①, reveals 3 main fiber directions at 45, 0 and -45 ° related to the geometry of the honeycomb pattern. More interesting is that even in the low dense areas, fibers are still highly orientated. As shown in **figures 3.4 and 3.5**, fibers are disposed along 0 ° and ±90 ° ④ or 0 ° and ±65 ° ⑤ directions. Alignment of fibers can be correlated to a similar process observed with a gap collection in electrospinning (Li et al., 2005; Qiao et al., 2018b; Shah Hosseini et al., 2018). Fibers are aligned along one direction to form a bridge between two conductive protrusions.

Average Fiber Diameters (AFD) were analyzed through SEM images (column 3 of **figure 3**). AFD depends on the location of fibers, decreasing from 3.1 µm to 2.2 µm in the zones ① and ⑤ respectively. **Figure 4.a** shows the AFDs trend regarding the different areas and the relative distance *d* between peaks of the micro-structured collectors. Distances $d_2$ to $d_5$ are described on the elementary honeycomb pattern in **figure 4.b**. The smallest diameter is obtained in the center of the mesh ⑤ where the space *d* between protrusions is maximum while AFD is maximum in the dense zone ①, similar to a random collection on flat surface (here considering as a conventional electrospinning i.e. $d = 0$). AFDs in zones ② and ③ are higher than the ones in zone ④ and ⑤, as the distance *d* between protrusions in ② and ③ is smaller. **Figure 4** exposes then the global tendency of AFD to decrease when the distance *d* increases.

This fiber diameter gradient is clearly related to the length of insulating gaps (here considering as the voids between protrusions). Vaquette et al. (Vaquette and Cooper-White, 2011) described than AFD is affected by the void gap length in their wire collectors. The first approach is that fibers elongate more as they have to make a longer path, resulting in a higher stretching and then in a lower fiber diameter. Another theory would rely on the non-regular morphology of the fiber during the deposition. Schlater et al. (Salima Nedjari et al., 2015) explained that structuration in electrospun scaffolds exhibiting beads and fibers is driven by

the bimodal character of the fiber. Following this approach, thicker segments of the fiber, with higher accumulated charge density, will be selectively attracted to very close protrusions and compose the main bridges observed in our honeycomb meshes. Low diameter fiber segments with lower charge density will deposit more randomly, filling the gaps of the honeycomb core.

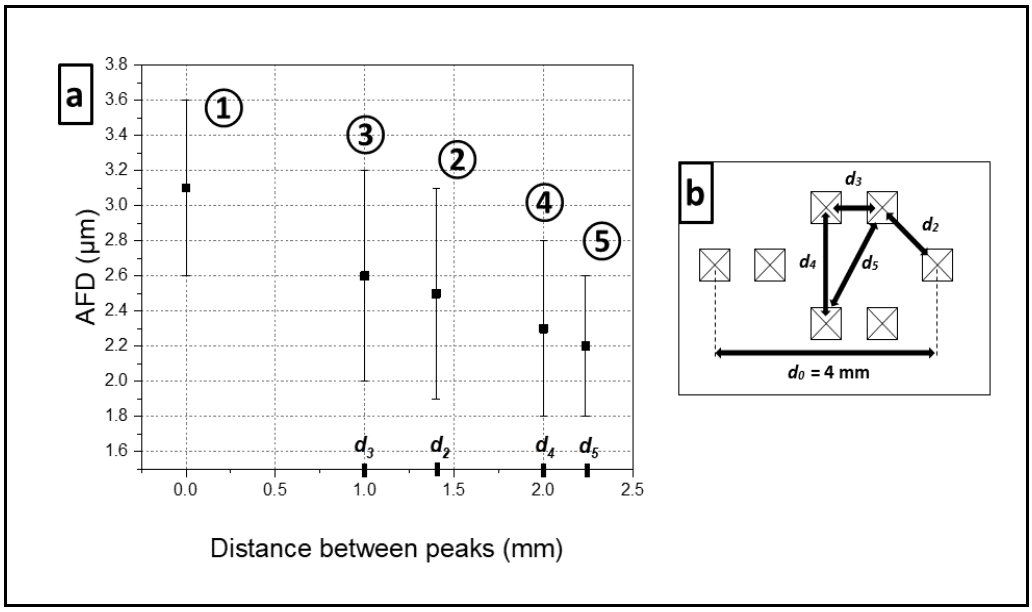


*Figure 4 – a) Average fiber diameter (AFD) of zones ① to ⑤ of the elementary honeycomb in function of the distance d between protrusions, b) definition of distances $d_1$ to $d_5$, $d_1$ for zone ① is considered as zero.*

### *3.3 Scaffold topology*

One of the main challenges mentioned in the literature in patterning electrospun scaffolds is to keep a well-defined fiber organization in depth. Indeed, fibers are collected onto the support and start to create an insulating or repulsive layer growing with time. Patterned structures usually vanish after a few minutes of collection, corresponding to few 100 µm layer of deposited fibers (Liu et al., 2014; Zhao et al., 2013). As a consequence, fibrous samples with well-defined architectures are relatively thin with a thickness that usually does not exceed 100 to 200 µm. Manipulation and subsequent tensile measurements of such membranes are not easy to perform, which might explain the poor mechanical characterization of patterned scaffolds in the literature.

**Figure 5.a** reveals the heterogeneous topography of the 3D structured fibrous mats via a 3D profilometer scan. **Figure 5.b** shows a SEM cross section view of the membrane, section being defined by the dashed line b in **Figure 5.a**. Honeycomb scaffolds are produced here over 70 mm with high and low fibers zones defining a 3D characteristic structure.

**Figure 5.c** shows the surface profile along the dashed line c in **figure 5.a**. Produced scaffolds displayed an apparent thickness between 350 and 500 µm, value of 381µm estimated in **figure 5**.

High thickness zones are situated on protrusions as more fibers are attracted and gathered onto these locations. Lowest thickness parts of the membrane are located in the centers of the patterns. Gaps between these high and low surface points are evaluated around 250 µm. Fibers are spatially arranged over a 15 to 30 min deposition time during which a distinct macrostructure is clearly preserved. The described method provides a better fiber structuration compared to usual electrospinning techniques with electro conductive templates in which a complete loss of fiber organization could be observed [36], [38].

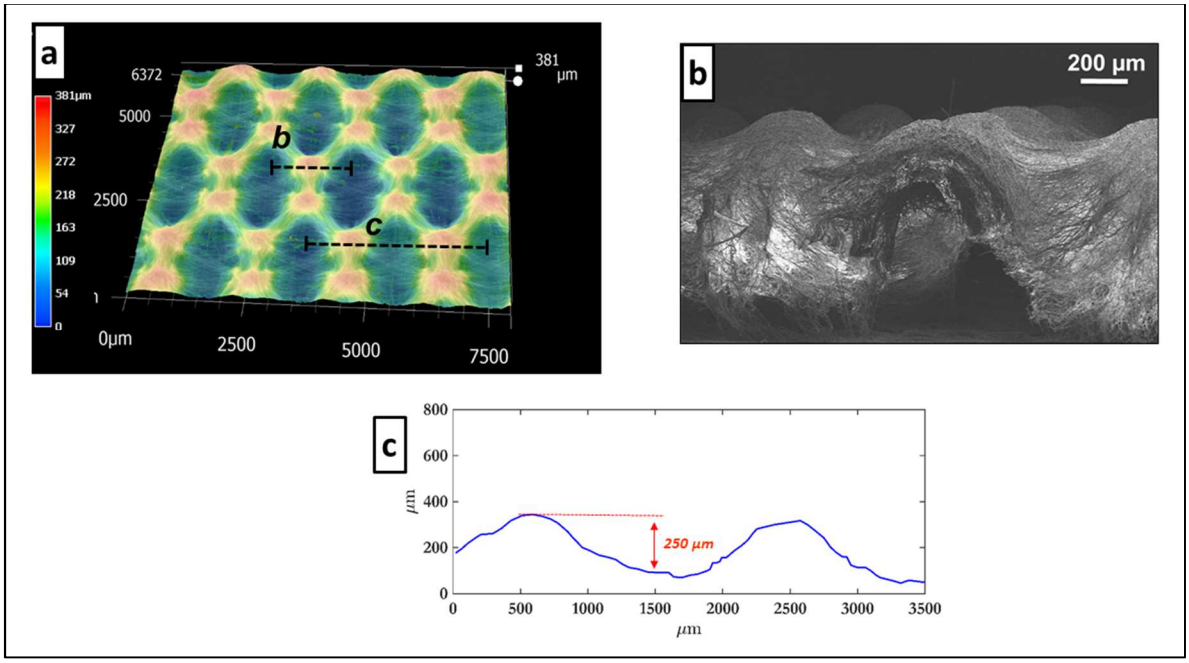


*Figure 5 – a) Optical profilometer scan of 3D honeycomb scaffolds, b) SEM image and c) profile graph of the membrane cross sections*

# 4. Tensile behavior - Monotonic large deformation loading

*4.1 Global stress-strain curves*

Mechanical tests were conducted on honeycomb patterned scaffolds in order to estimate the influence of the microstructure on mechanical behaviors. Axial tensile tests were first performed on the honeycomb structures along two directions, $D_1$ and $D_2$ (see **figure 2**). **Figure 6** displays tensile curves of the honeycomb fibrous mats. The nominal stress, calculated from **equation (2)**, is plotted in function of the global true strain defined as $\ln(^{H}/_{H_0})$. Standard deviations are depicted with blurred zones in **figure 6**. Pictures of deformed membranes are illustrated in the two directions $D_1$ and $D_2$ at 0, 15, 30 and 50% of global true strain.

Curves show a classic "stress-strain" like shape, beginning by a quasi linear part at low strain (until approximately 15 % for $D_1$ and 30 % for $D_2$) and followed by a plateau. This two steps behavior is specific of fibrous polymer materials (Ridruejo et al., 2011; Sinha-Ray et al., 2014). Failure was observed in the case of $D_1$ direction around 55 % of global true strain. With $D_2$ patterns, a maximum strain of 130 % was reached before complete rupture of fibers (maximum apparatus gap of the test bench). Rupture of the membranes occurred always at the vicinity of the grips.

Slope in the first linear part, indicated here as modulus $E$, is significantly higher for the $D_1$ orientation, $E_1 = 1.7 \pm 0.1$ MPa versus $E_2 = 0.4 \pm 0.1$ MPa for $D_2$. Such values of modulus are slightly lower that the ones found in the literature of PCL patterned scaffolds collected on metals grids (2 to 4 MPa for Vaquette et al (Vaquette and Cooper-White, 2011) or 5 to 10 MPa for Wang et al (Yazhou Wang et al., 2009)). This difference with literature in scaffold stiffness might be explained by several factors such as a higher average fiber diameter, a higher global porosity or a more important heterogeneity in the fibrous network with more distinct areas of high and low fiber density. Yield Strains delimit the first linear regime and the second plateau regime, i.e. where the first part of the curve becomes markedly nonlinear. They were evaluated on the basis of 2 % strain difference between the straight line and the actual curve. Tensile tests performed in the $D_2$ direction display a high yield strain of 38 % whereas in $D_1$ direction, yield point is reached at a lower value of 19 % (**figure 6**).

Anisotropic ratio, $E_1/E_2$ of moduli of the first linear part, has a value of 4.2 proving the strong anisotropic behavior of produced mats. Such difference in axial stresses between $D_1$ and $D_2$ directions is due to the structural fibers orientation of the honeycomb configuration. Similar results on mechanical properties were obtained with fibers collecting on a metallic screw, producing a significant anisotropy ratio of 3.4 between axial and transverse directions (Neves et al., 2007). Such value of anisotropic ratio is in good accordance with most natural soft tissues (human skin, tendons, ligaments, muscular tissues) found in the human body (anisotropy between 3 to 5) (Manschot and Brakkee, 1986), showing that our strategy to reproduce natural anisotropy is appropriated and can be used for soft tissue engineering applications.

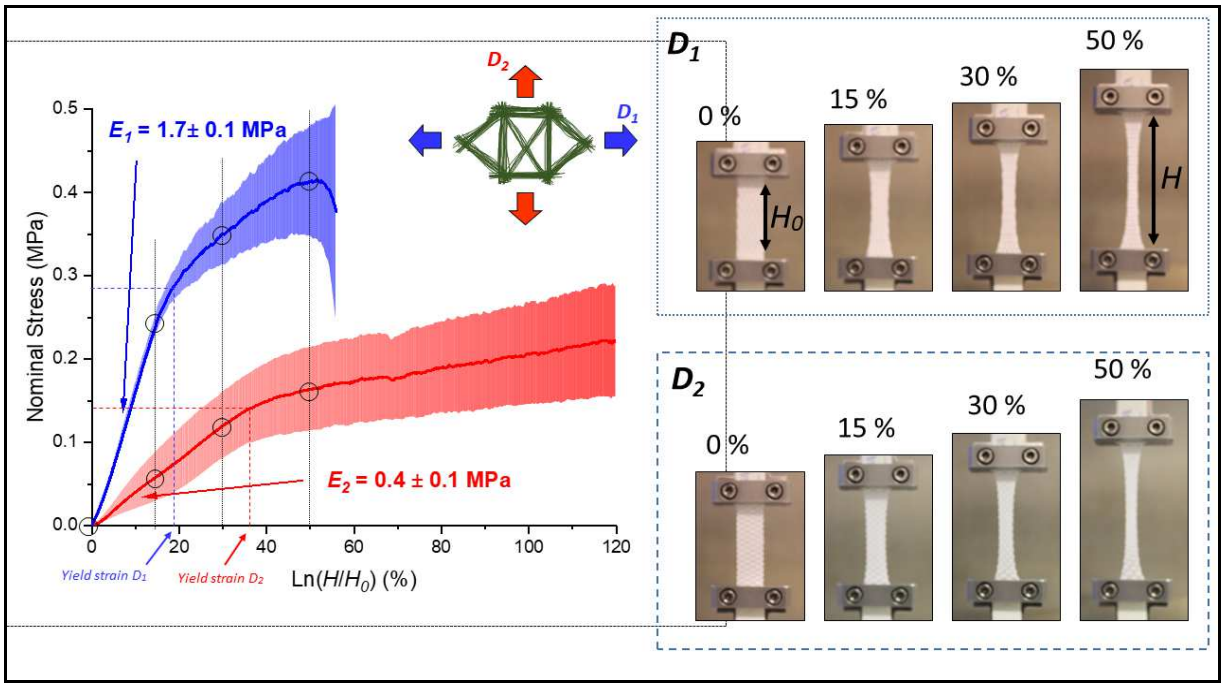


*Figure 6 – Average Nominal Stress with standard deviations vs global True Strain of honeycomb PCL scaffolds. Pictures of tensile test in $D_1$ and $D_2$ directions at 0, 15, 30 and 50 % of global true strain*

### *4.2 Local and Global axial strains*

Global strain analysis does not consider the heterogeneous deformation of the fibrous tensile sample shown in the deformed pictures in **figure 6**. In order to analyze the influence of the microstructure on anisotropic behaviors of honeycomb scaffolds $D_1$ and $D_2$, local

deformations at the center of the sample were investigated during tensile test. **Figure 7** shows sets of images of the single honeycomb mesh during elongation along $D_1$ and $D_2$ directions. Images of the deformed patterns were taken by a digital camera always focused at the center of the gauge length of tensile samples. Local axial and transverse true strains in $D_1$ and $D_2$ directions (see expressions in **figure 7**) were extracted from the sequence of images. Distances $d_0$ and $d_4$ were measured and averaged over 3 different patterns for each image of the sequence to calculate transverse and axial local strains.

Images after 40 % of global true strain were not exploited due to a loss of contrast or a loss of the visual monitoring of the protrusions. Plot in **figure 7** displays the Nominal Stress versus the global (dashed lines) and calculated local (full lines) true strains.

The difference between local and global strains is low until a critical value of 15 % for $D_1$ direction and 30 % for $D_2$ direction. In these domains, local analysis is matching the global strain behavior. However, after critical values, corresponding to higher strains, the local strain gives a more accurate understanding of the scaffold mechanical behavior.

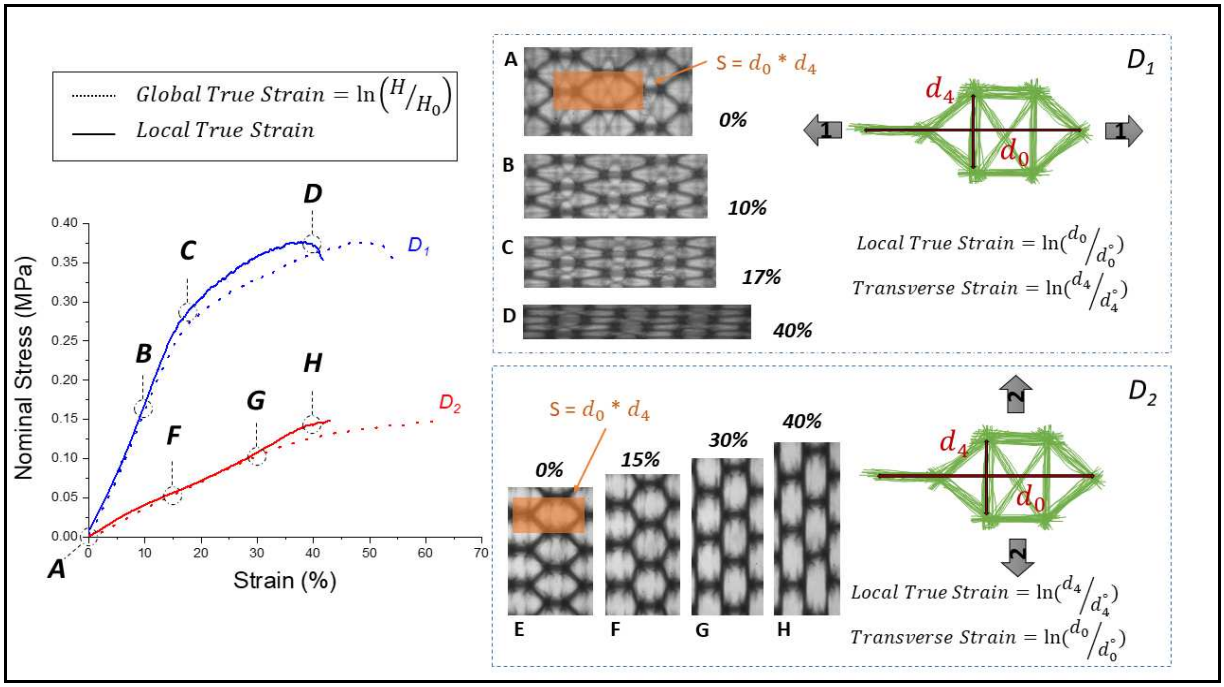


*Figure 7 – Nominal stress of honeycomb scaffolds in function of global (dashed line) or local true strains (solid line). Optical images of $D_1$ and $D_2$ scaffolds at different global true strains. Surface $S = d_0 * d_5$ is plotted in color orange*

*4.3 Transverse versus axial strains*

**Figure 8.a** exhibits the link between the axial (local true strain) and transverse strains in $D_1$ and $D_2$ configurations. Both values of the transverse strain are negative, which indicates a contraction of the material in the perpendicular direction. Honeycomb scaffolds expose a higher overall transverse strain in $D_1$ direction compared to $D_2$ direction. This difference of the membrane contraction during stretching is a direct consequence of scaffold microstructure. The honeycomb fiber network induces a stronger transverse resistance in $D_2$ direction. As $D_1$ tensile test samples are more contracted along the transverse direction, higher stresses will be applied at the vicinity of the grips. This phenomenon would explain the failure observed at a shorter elongation in $D_1$ direction (**figure 6**), due to a higher restriction nearby the grips. Moreover, the higher transverse contraction of the scaffolds in direction $D_2$ will induce a stronger fiber densification, which would explain a higher stress of $D_2$ scaffolds measured in **figure 6**. Indeed, as shown by Silberstein et al, transverse contraction while stretching is directly linked to a change in porosity. Fibers organized and aligned in the direction of loading increasing the mechanical stiffness of the mats (**figure 6**).

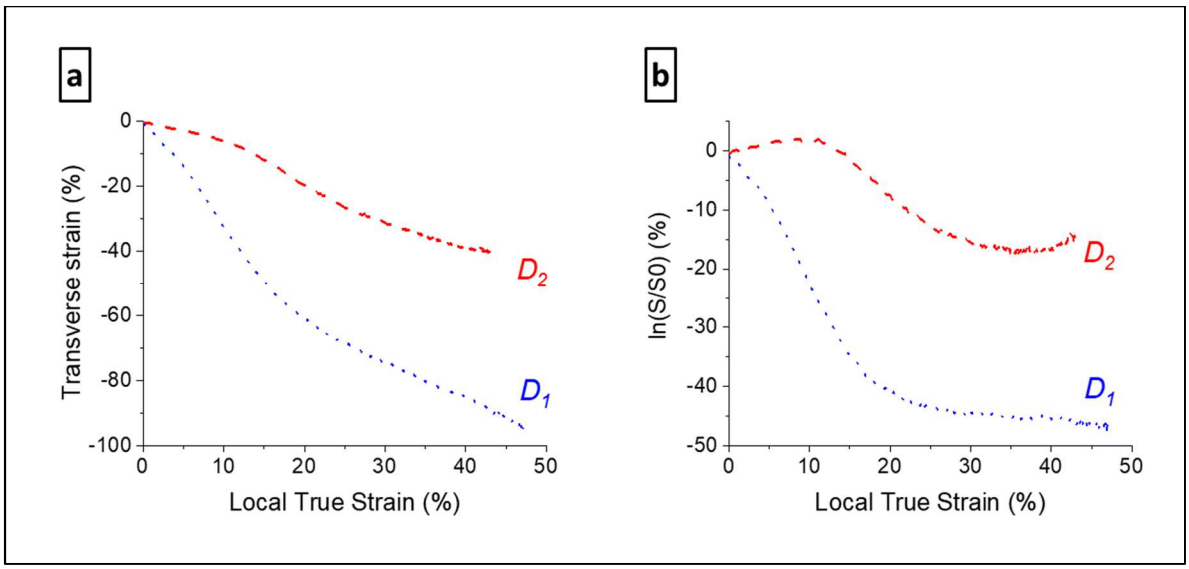


*Figure 8 - Local deformation of a single honeycomb mesh ($D_1$ and $D_2$ directions), a) Transverse strain versus Local True Strain, b) local relative variation of the surface*

**Figure 8.b** shows the local relative variation of the surface $\ln(S/S_0)$ of an elementary honeycomb pattern during stretching. The elementary surface $S = d_0 * d_4$ is plotted in orange in **figure 7** on the initial image of honeycomb scaffolds. This relative variation is simply calculated from the sum of the local axial and transverse true strains. A reduction of surface ($\ln\left(S/S_0\right) < 0$) in the $D_1$ direction is observed up to a maximum of -45 %. In $D_2$ direction, the surface of the mesh initially increases weakly up to an axial strain of 17 % and then decreases gradually, leading to a relative surface reduction of – 15 %. The evolution of relative variation of the surface clearly exposes the anisotropic behavior of honeycomb scaffolds. The geometry of the mesh induces a distinct mechanical answer depending on the load directions. **Figure 8.a and b** characterize accurately the local anisotropic mechanical answers of the one honeycomb pattern. This analysis can be very useful to propose constitutive equations of one pattern considered as a representative Elementary Volume and thus to model by finite element simulation the mechanical behavior of a scaffold constituted of several patterns.

## 5. Tensile behavior – Monotonic small deformation loading

Mechanical behaviors present two regimes in terms of stress and local strain answers at low and high strains. Curves in **figures 7 and 8** expose a quasi linear regime in $D_1$ and $D_2$ directions until 15 % of axial strains. Considering that scaffolds for biomedical applications (skin (Maiti et al., 2016), ligament (Ruspi et al., 2020) or bone (Ahmed et al., 2020) implants) would endure relatively small local strains, this last section will detail the mechanical behavior of honeycomb scaffolds in the first 15 % of true strain corresponding to the first linear regime. However, it has to be noticed that scaffolds can stand a true strain of about 40% without breaking.

In a first part, viscosity of the membranes is investigated through stress relaxation tests to determine the elasticity properties of these first linear regimes. Then, an orthotropic elastic model is introduced to describe the mechanical behavior at low strain of the honeycomb mats.

*5.1 Relaxation*

Relaxation of the honeycomb scaffolds was firstly investigated in both directions $D_1$ and $D_2$. **Figure 9.a** shows the measurement of nominal stress with a two steps strain control experiment. Scaffolds were extended at a fixed strain rate of 3.3 $10^{-3}$ $s^{-1}$ in order to reach a maximum strain of 15 %. Then strain was kept constant to examine the relaxation of the polymer membrane at 15 % for 45 seconds, time length considered sufficiently long to observe and fit correctly the relaxation curves. As illustrated in **figure 9.a**, scaffolds exhibit in both directions a small relaxation proving that the viscosity of the material will not drastically influence the mechanical behaviors. At the end of a 45 s loading, ratio between the maximal stress values $\sigma_{max\ D1}/\sigma_{max\ D2}$ (t=45s) is equal to 4.1 . The stress ratio is preserved after relaxation at $t=90\ s$ $\sigma_{inf\ D1}/\sigma_{inf\ D2} = 4.2$ showing that relaxation of the polymer is sufficiently low and preserve the anisotropic properties of the scaffolds.

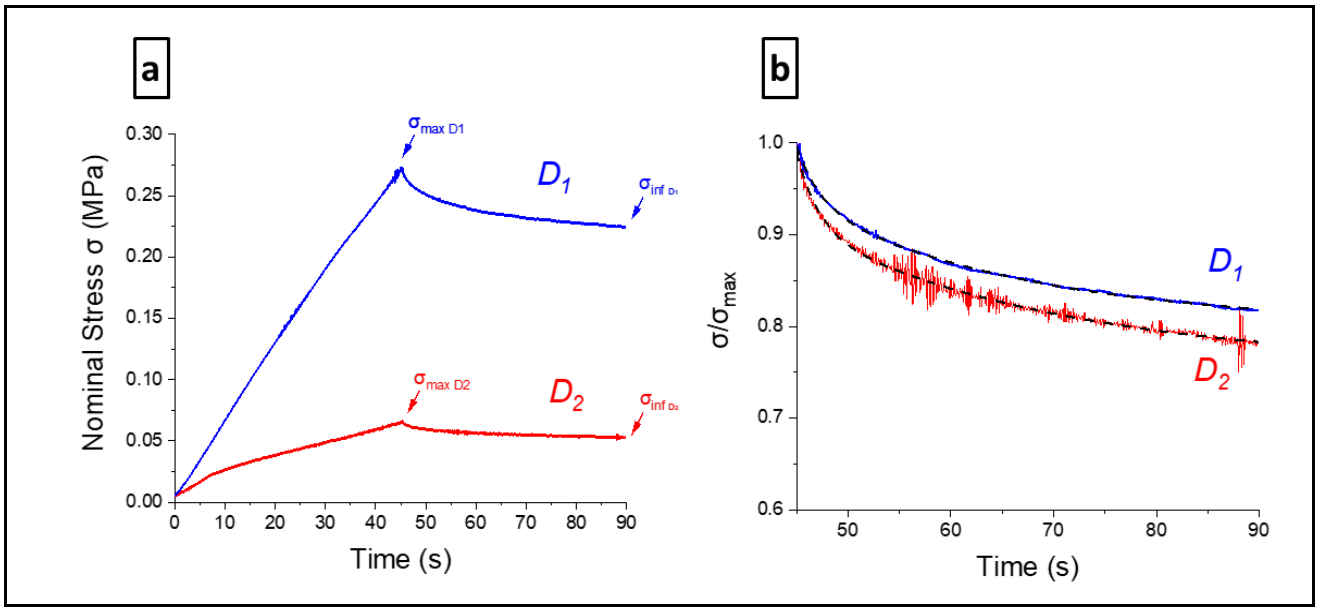


*Figure 9 - a) Charge of honeycomb scaffolds in $D_1$ and $D_2$ directions b) Stress relaxation curves: Nominal stress normalized by its highest value $\sigma_{max}$ reached at t = 45 s, dashed black curves represented the fit equation (3)*

Normalized stress relaxation curves of $D_1$ and $D_2$ honeycomb scaffolds are plotted on **figure 9.b**. Nominal stresses are normalized respectively with their highest values $\sigma_{max}$ reached at t = 45 s, beginning of the relaxation. Both curves adopted a similar trend which can be properly fitted with a double exponential **equation (3):**

$$\sigma(t)/\sigma_{max} = a\, e^{-t/\tau_1} + b\, e^{-t/\tau_2} + \sigma_\infty \quad (3)$$

The relaxation parameters are exposed in **table 1.** The time-dependent response of these electrospun materials are well described by this 5 parameters generalized Maxwell model, employed to model electrospun scaffolds (Sethuraman et al., 2013; Waheed et al., 2018) or natural tissue relaxation (Machiraju et al., 2006).

| | ***Short relaxation time $\tau_1$ (s)*** | ***Long relaxation time $\tau_2$ (s)*** | ***Normalized infinite Stress $\sigma_\infty$*** |
|---|---|---|---|
| *Direction $D_1$* | *2.2* | *22* | *0.8* |
| *Direction $D_2$* | *2.1* | *26* | *0.76* |

*Table 1 – Relaxation parameters of electrospun honeycomb patterned membranes*

Short and long relaxation times $D_1$ and $D_2$ differ from one order of magnitude. The fast relaxation $\tau_1$ time might be attributed to the local deformation of fibers while slow relaxation time $\tau_2$ could reflect the constrained molecular dynamics of stretched polymer chains. Similar observations were collected when fitting stress relaxation of electrospun fibers by a same 5 parameters model (Baker et al., 2012; Waheed et al., 2018). Relaxation parameters are quasi identical for the two directions of elongation $D_1$ and $D_2$ which means that the viscoelastic relaxation dynamics are independent of the tensile direction. Infinite stress or equilibrium stress, is estimated around 80 %, proving that materials still have a consistent structural answer under an imposed constant strain. Therefore, viscous properties of the produced honeycomb scaffolds were neglected for a further detailed description of the mechanical behaviors.

### *5.2 Orthotropic elastic model of one pattern*

A single honeycomb pattern is modeled here mechanically as it can be assimilated as a representative Elementary volume of a bigger structural scaffolds. Developing constitutive equations for one single pattern will provide the initial elements to develop a finite element model of a more complex scaffold made of several patterns.

Considering the low viscosity properties analyzed in the paragraph above, a linear elastic model is proposed in this section to describe the anisotropic mechanical behavior of the honeycomb scaffolds considered as membranes. This model is valid only at small deformation where the linear regimes were observed experimentally.

A strict linear elasticity model is employed in which the following Hooke's law might be used:

$$\begin{bmatrix}\sigma_{11}\\ \sigma_{22}\\ \sigma_{12}\end{bmatrix} = C \begin{bmatrix}\varepsilon_{11}\\ \varepsilon_{22}\\ 2\varepsilon_{12}\end{bmatrix} \; with\; C = \begin{bmatrix}C_{11} & C_{12} & C_{13}\\ C_{21} & C_{22} & C_{23}\\ C_{31} & C_{32} & C_{33}\end{bmatrix} \qquad (4)$$

The 3x3 elasticity symmetric tensor $C$ relates the stress $\sigma$ and the strain $\varepsilon$ via the **equation (4)**, where $\sigma$ and $\varepsilon$ have 3 values referring to *11*, *22* normal components and *12* shear components. In the case of orthotropic materials, the normal and shear components are decoupled meaning that normal stresses only cause normal strains and shear stresses only cause shear strains. Elasticity tensor can be simplified with only 5 free parameters:

$$\mathrm{C}_{ortho} = \begin{bmatrix}C_{11} & C_{12} & 0\\ C_{21} & C_{22} & 0\\ 0 & 0 & C_{33}\end{bmatrix} \qquad (5)$$

It is simpler to define the inverse elasticity tensor ${\mathrm{C}_{ortho}}^{-1}$, which can be expressed as following:

$$\begin{bmatrix}\varepsilon_{11}\\ \varepsilon_{22}\\ 2\varepsilon_{12}\end{bmatrix} = \begin{bmatrix}{}^{1}/_{E_1} & -{}^{\upsilon_{12}}/_{E_1} & 0\\ -{}^{\upsilon_{21}}/_{E_2} & {}^{1}/_{E_2} & 0\\ 0 & 0 & {}^{1}/_{\mu_{12}}\end{bmatrix} \begin{bmatrix}\sigma_{11}\\ \sigma_{22}\\ \sigma_{12}\end{bmatrix} \qquad (6)$$

with $E$ Young moduli, $\upsilon$ Poisson's coefficients and $\mu$ shear modulus

**Figure 10** exposes experimental curves needed to retrieve the specific mechanical properties required to complete the 2D orthotropic mechanical model. Axial mechanical tests **figure 10.a** and local strain analysis **figure 10.b** of the honeycomb scaffolds give all required information to characterize the anisotropy of the architected scaffolds. Linear regimes for

these two figures are observed experimentally from 0 to 10% of true strain, in which the present elastic model might be verified and applied.

From the nominal stress analysis in **figure 10.a**, Young's moduli $E_1$ and $E_2$ in two directions are extracted, from a linear fit from 0 to 10% of true strain.

**Figure 10.b** shows the local transverse strain curves. Poisson's coefficients are calculated ($\upsilon_{12} = 3.5 \pm 0.4$ and $\upsilon_{21} = 0.6 \pm 0.1$) on the same linear regime. Poisson's ratio $\upsilon_{ij}$ (for $i \neq j$) gives the contraction in direction $j$ when the extension is applied in direction $i$. The behavior of the local transverse strains is rigorously linear for both directions until 10 % of local true strain, proving that the model might be theoretically valid for small deformations. It can be added than the contraction behavior is less pronounced in random membranes (Poisson coefficient of 0.46 for PCL electrospun mats [ref de Bhullar]). Patterned honeycomb scaffolds contains areas of low fibers density which allow a greater transverse contraction of the membranes.

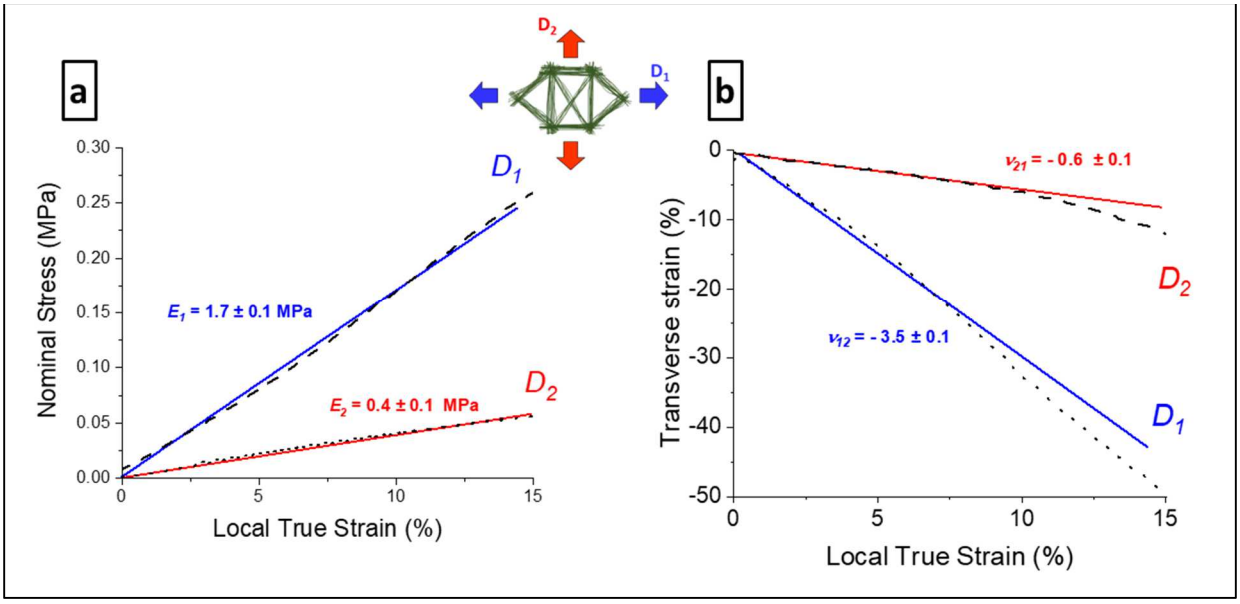


*Figure 10 - a) Nominal stress and b) Transverse strain at small deformations, linear fits are calculated for values of true strain comprised between 0 to 15%*

**Table 2** lists all required mechanical properties to fulfill the elasticity tensor. Young's moduli and Poisson's ratios were measured from the previous experimental curves. Experimental shear test was not feasible considering the small thickness of the samples. Consequently, last shear modulus value $\mu_{12}$ was estimated via the Huber's formula (7) (Huber M., 1923).

| $E_1$ | $E_2$ | $\upsilon_{12} = -\frac{\varepsilon_{22}}{\varepsilon_{11}}$ | $\upsilon_{21} = -\frac{\varepsilon_{11}}{\varepsilon_{22}}$ | $\mu_{12} = \frac{\sqrt{E_1 E_2}}{2(1+\sqrt{\upsilon_{12}\upsilon_{21}})}$ (7) |
|---|---|---|---|---|
| $1.7 \pm 0.1$ MPa | $0.4 \pm 0.1$ MPa | $3.5 \pm 0.4$ | $0.6 \pm 0.1$ | $0.16 \pm 0.05$ MPa |

*Table 2 – Mechanical parameters of electrospun PCL honeycomb scaffolds*

For an orthotropic linear model, the inverse elasticity tensor ${C_{ortho}}^{-1}$ is defined symmetric. Thus, a relation (7) between Young's moduli and Poisson's coefficients can be deduced from the expression of ${C_{ortho}}^{-1}$ **in equation (6)**.

The following **equation (8)** needs to be verified to insure the symmetry of the tensor ${C_{ortho}}^{-1}$:

$$\frac{\upsilon_{12}}{E_1} = \frac{\upsilon_{21}}{E_2} \quad (8)$$

These ratios were experimentally calculated from the parameters of **table (2)**:

$$\frac{\upsilon_{12}}{E_1} = 2.1 \pm 0.4 \text{ and } \frac{\upsilon_{21}}{E_2} = 1.6 \pm 0.7 \ (9)$$

The disparity between the 2 ratios is relatively small and **equation (8)** is verified taking into account the relative errors made experimentally, induced either by the replicability of the tests or the local strain measurements. These experimental calculations reinforces the use of an orthotropic linear elastic model to represent the honeycomb mechanical behavior.

This first model of the honeycomb mats is a strong first approach in the description and future development of applied regeneration scaffolds with more complex loading constraints.

## 6. Conclusion

A new way to shape by electrospinning scaffolds with anisotropic properties was investigated in this study. Honeycomb patterned fibrous mats were successfully produced by electrospinning using new template-assisted collectors. The metal 3D collectors allowed the fabrication of well-shaped anisotropic hexagonal honeycombs. Fibers observe different

average diameters, densities and orientations depending on the regions in the elementary honeycomb pattern. Mechanical tensile tests confirmed the anisotropic nature of the produced scaffolds at small and large strains. Anisotropic ratio of elastic moduli of 4.2 was found between transverse and axial directions, matching to the range of soft tissue structural properties. At small strains (up to 10%) where the viscosity aspect can be neglected, an orthotropic linear elastic model was introduced to depict the anisotropic mechanical behavior of the micro-structured scaffolds. For future biomedical applications, the produced honeycomb meshwork will give the mechanical stability needed while the center of the mesh, niche with high porosity and good pore interconnection, will create a friendly environment to host cells. The illustrated electrospinning process will provide promising tools to regenerative medicine to create artificial scaffolds to replace anisotropic targeted tissues.

## Acknowledgement

The authors gratefully acknowledge M. Karrouch for the assistance in the elaboration of the microstructured collectors and R. Martin for her expertise and assistance in SEM microscopy. The present work was partially supported by the ANR2016-BIOSCAFF (ANR-16-CE09-0024) held by the University of Grenoble-Alpes.

# References

Ahirwal, D., Hébraud, A., Kádár, R., Wilhelm, M., Schlatter, G., 2013. From self-assembly of electrospun nanofibers to 3D cm thick hierarchical foams. Soft Matter 9, 3164. https://doi.org/10.1039/c2sm27543k

Ahmed, K., Greene, R.J., Aston, W., Briggs, T., Pendegrass, C., Moazen, M., Blunn, G., 2020. Experimental Validation of an ITAP Numerical Model and the Effect of Implant Stem Stiffness on Bone Strain Energy. Ann Biomed Eng 48, 1382–1395. https://doi.org/10.1007/s10439-020-02456-6

Alfaro De Prá, M.A., Ribeiro-do-Valle, R.M., Maraschin, M., Veleirinho, B., 2017. Effect of collector design on the morphological properties of polycaprolactone electrospun fibers. Materials Letters 193, 154–157. https://doi.org/10.1016/j.matlet.2017.01.102

Baker, S., Sigley, J., Helms, C.C., Stitzel, J., Berry, J., Bonin, K., Guthold, M., 2012. The mechanical properties of dry, electrospun fibrinogen fibers. Materials Science and Engineering: C 32, 215–221. https://doi.org/10.1016/j.msec.2011.10.021

Bayati, V., Altomare, L., Tanzi, M.C., Farè, S., 2013. Adipose-derived stem cells could sense the nano-scale cues as myogenic-differentiating factors. J Mater Sci: Mater Med 24, 2439–2447. https://doi.org/10.1007/s10856-013-4983-5

Beachley, V., 2011. Effect of electrospinning parameters on the nanofiber diameter and length 17.

Beachley, V., Wen, X., 2009. Effect of electrospinning parameters on the nanofiber diameter and length. Materials Science and Engineering: C 29, 663–668. https://doi.org/10.1016/j.msec.2008.10.037

Chou, S.-F., Woodrow, K.A., 2017. Relationships between mechanical properties and drug release from electrospun fibers of PCL and PLGA blends. Journal of the Mechanical Behavior of Biomedical Materials 65, 724–733. https://doi.org/10.1016/j.jmbbm.2016.09.004

Criscenti, G., Vasilevich, A., Longoni, A., De Maria, C., van Blitterswijk, C.A., Truckenmuller, R., Vozzi, G., De Boer, J., Moroni, L., 2017. 3D screening device for the evaluation of cell response to different electrospun microtopographies. Acta Biomaterialia 55, 310–322. https://doi.org/10.1016/j.actbio.2017.03.049

Croisier, F., Duwez, A.-S., Jérôme, C., Léonard, A.F., van der Werf, K.O., Dijkstra, P.J., Bennink, M.L., 2012. Mechanical testing of electrospun PCL fibers. Acta Biomaterialia 8, 218–224. https://doi.org/10.1016/j.actbio.2011.08.015

Daming, Z., Jiang, C., 2008. Electrospinning of Three-Dimensional Nanofibrous Tubes with Controllable Architectures. Nano Letters 8, 3283–3287.

Dippold, D., Cai, A., Hardt, M., Boccaccini, A.R., Horch, R., Beier, J.P., Schubert, D.W., 2017. Novel approach towards aligned PCL-Collagen nanofibrous constructs from a benign solvent system. Materials Science and Engineering: C 72, 278–283. https://doi.org/10.1016/j.msec.2016.11.045

Domaschke, S., Morel, A., Kaufmann, R., Hofmann, J., Rossi, R.M., Mazza, E., Fortunato, G., Ehret, A.E., 2020. Predicting the macroscopic response of electrospun membranes based on microstructure and single fibre properties. Journal of the Mechanical Behavior of Biomedical Materials 104, 103634. https://doi.org/10.1016/j.jmbbm.2020.103634

Engelmayr, G.C., Cheng, M., Bettinger, C.J., Borenstein, J.T., Langer, R., Freed, L.E., 2008. Accordion-like honeycombs for tissue engineering of cardiac anisotropy. Nature Materials 7, 1003–1010. https://doi.org/10.1038/nmat2316

Flemming, R.G., Murphy, C.J., Abrams, G.A., Goodman, S.L., Nealey, P.F., 1999. Effects of synthetic micro- and nano-structured surfaces on cell behavior. Biomaterials 20, 573–588. https://doi.org/10.1016/S0142-9612(98)00209-9

Fung, Y.-C., 1995. Stress, Strain, growth, and remodeling of living organisms, in: Casey, J., Crochet, M.J. (Eds.), Theoretical, Experimental, and Numerical Contributions to the Mechanics of Fluids and Solids. Birkhäuser Basel, Basel, pp. 469–482. https://doi.org/10.1007/978-3-0348-9229-2_25

Garcia Garcia, A., Hébraud, A., Duval, J.-L., Wittmer, C.R., Gaut, L., Duprez, D., Egles, C., Bedoui, F., Schlatter, G., Legallais, C., 2018. Poly(ε-caprolactone)/Hydroxyapatite 3D Honeycomb Scaffolds for a Cellular Microenvironment Adapted to Maxillofacial Bone Reconstruction. ACS Biomaterials Science & Engineering 4, 3317–3326. https://doi.org/10.1021/acsbiomaterials.8b00521

George, J., Kuboki, Y., Miyata, T., 2006. Differentiation of mesenchymal stem cells into osteoblasts on honeycomb collagen scaffolds. Biotechnol. Bioeng. 95, 404–411. https://doi.org/10.1002/bit.20939

Huber M., 1923. The theory of crosswise reinforced ferroconcrete slabs and its application to various important constructional problems involving rectangular slabs. Der Bauingenieur4 354–360.

Jamadi, E.S., Ghasemi-Mobarakeh, L., Morshed, M., Sadeghi, M., Prabhakaran, M.P., Ramakrishna, S., 2016. Synthesis of polyester urethane urea and fabrication of elastomeric nanofibrous scaffolds for myocardial regeneration. Materials Science and Engineering: C 63, 106–116. https://doi.org/10.1016/j.msec.2016.02.051

Janmohammadi, M., Nourbakhsh, M.S., 2019. Electrospun polycaprolactone scaffolds for tissue engineering: a review. International Journal of Polymeric Materials and Polymeric Biomaterials 68, 527–539. https://doi.org/10.1080/00914037.2018.1466139

Kang, Y., Chen, P., Shi, X., Zhang, G., Wang, C., 2018. Multilevel structural stereocomplex polylactic acid/collagen membranes by pattern electrospinning for tissue engineering. Polymer 156, 250–260. https://doi.org/10.1016/j.polymer.2018.10.009

Katsube, N., Lannutti, J., Duling, R.R., Dupaix, R.B., 2008. Mechanical Characterization of Electrospun Polycaprolactone (PCL): A Potential Scaffold forTissue Engineering. Journal of Biomechanical Engineering 130, 13.

Kuppan, P., Sethuraman, S., Krishnan, U.M., 2017. In vitro co-culture of epithelial cells and smooth muscle cells on aligned nanofibrous scaffolds. Materials Science and Engineering: C 81, 191–205. https://doi.org/10.1016/j.msec.2017.07.050

Lancuški, A., Bossard, F., Fort, S., 2013. Carbohydrate-Decorated PCL Fibers for Specific Protein Adhesion. Biomacromolecules 14, 1877–1884. https://doi.org/10.1021/bm400263d

Lancuški, A., Fort, S., Bossard, F., 2012. Electrospun Azido-PCL Nanofibers for Enhanced Surface Functionalization by Click Chemistry. ACS Applied Materials & Interfaces 4, 6499–6504. https://doi.org/10.1021/am301458y

Lee, K.H., Kim, H.Y., Khil, M.S., Ra, Y.M., Lee, D.R., 2003. Characterization of nano-structured poly(1-caprolactone) nonwoven mats via electrospinning 8.

Li, D., Ouyang, G., McCann, J.T., Xia, Y., 2005. Collecting Electrospun Nanofibers with Patterned Electrodes. Nano Letters 5, 913–916. https://doi.org/10.1021/nl0504235

Li, D., Wang, Y., 2003. Electrospinning of Polymeric and Ceramic Nanofibers as Uniaxially Aligned Arrays. Nano Lett. 3, 5.

Li, Y., Zhang, C., Zhu, L. -F., Ahmad, Z., Li, J. -S., Chang, M. -W., 2019. Elastic antibacterial membranes comprising particulate laden fibers for wound healing applications. Journal of Applied Polymer Science 136, 47105. https://doi.org/10.1002/app.47105

Liu, L., Dzenis, Y.A., 2008. Analysis of the Effects of the Residual Charge and Gap Size on Electrospun Nanofiber Alignment in a Gap Method 8.

Liu, S.L., Sun, G.H., Huang, Y.Y., Sun, B., Zhang, H.D., Long, Y.Z., 2014. Fabrication and Formation Mechanism of Electrospun Spatially Defined Fibrous Patterning Structures on Conductive and Insulating Substrates. Key Engineering Materials 609–610, 842–848. https://doi.org/10.4028/www.scientific.net/KEM.609-610.842

Ma, P.X., 2008. Biomimetic materials for tissue engineering. Advanced Drug Delivery Reviews 60, 184–198. https://doi.org/10.1016/j.addr.2007.08.041

Machiraju, C., Phan, A.-V., Pearsall, A.W., Madanagopal, S., 2006. Viscoelastic studies of human subscapularis tendon: Relaxation test and a Wiechert model. Computer Methods and Programs in Biomedicine 83, 29–33. https://doi.org/10.1016/j.cmpb.2006.05.004

Maiti, R., Gerhardt, L.-C., Lee, Z.S., Byers, R.A., Woods, D., Sanz-Herrera, J.A., Franklin, S.E., Lewis, R., Matcher, S.J., Carré, M.J., 2016. In vivo measurement of skin surface strain and sub-surface layer deformation induced by natural tissue stretching. Journal of the Mechanical Behavior of Biomedical Materials 62, 556–569. https://doi.org/10.1016/j.jmbbm.2016.05.035

Manschot, J.F.M., Brakkee, A.J.M., 1986. The measurment and modelling of the mechanical properties of human skin in vivo-II. The model. J. Biomechanics 19, 517–521.

Munir, M.M., Widiyandari, H., Iskandar, F., Okuyama, K., 2008. Patterned indium tin oxide nanofiber films and their electrical and optical performance. Nanotechnology 19, 375601. https://doi.org/10.1088/0957-4484/19/37/375601

Nedjari, S., Hébraud, A., Eap, S., Siegwald, S., Mélart, C., Benkirane-Jessel, N., Schlatter, G., 2015. Electrostatic template-assisted deposition of microparticles on electrospun nanofibers: towards microstructured functional biochips for screening applications. RSC Advances 5, 83600–83607. https://doi.org/10.1039/C5RA15931H

Nedjari, Salima, Schlatter, G., Hébraud, A., 2015. Thick electrospun honeycomb scaffolds with controlled pore size. Materials Letters 142, 180–183. https://doi.org/10.1016/j.matlet.2014.11.118

Neves, N.M., Campos, R., Pedro, A., Cunha, J., Macedo, F., Reis, R.L., 2007. Patterning of polymer nanofiber meshes by electrospinning for biomedical applications. Internation Journal of Nanomedicine 433–448.

Ní Annaidh, A., Bruyère, K., Destrade, M., Gilchrist, M.D., Otténio, M., 2012. Characterization of the anisotropic mechanical properties of excised human skin. Journal of the Mechanical Behavior of Biomedical Materials 5, 139–148. https://doi.org/10.1016/j.jmbbm.2011.08.016

O'Brien, F.J., 2011. Biomaterials & scaffolds for tissue engineering. Materials Today 14, 88–95. https://doi.org/10.1016/S1369-7021(11)70058-X

Püspöki, Z., Storath, M., Sage, D., Unser, M., 2016. Transforms and Operators for Directional Bioimage Analysis: A Survey. Adv Anat Embryol Cell Biol 219, 69–93.

Qiao, Y., Liu, X., Fu, G., He, Z., Hou, C., Li, Y., Zhang, Q., Yan, H., Wang, H., 2018a. An ordered electrospun polycaprolactone–collagen–silk fibroin scaffold for hepatocyte culture. Journal of Materials Science 53, 1623–1633. https://doi.org/10.1007/s10853-017-1670-9

Qiao, Y., Liu, X., Fu, G., He, Z., Hou, C., Li, Y., Zhang, Q., Yan, H., Wang, H., 2018b. An ordered electrospun polycaprolactone–collagen–silk fibroin scaffold for hepatocyte culture. Journal of Materials Science 53, 1623–1633. https://doi.org/10.1007/s10853-017-1670-9

Ridruejo, A., González, C., LLorca, J., 2011. Micromechanisms of deformation and fracture of polypropylene nonwoven fabrics. International Journal of Solids and Structures 48, 153–162. https://doi.org/10.1016/j.ijsolstr.2010.09.013

Rogers, C.M., Morris, G.E., Gould, T.W.A., Bail, R., Toumpaniari, S., Harrington, H., Dixon, J.E., Shakesheff, K.M., Segal, J., Rose, F.R.A.J., 2014. A novel technique for the production of electrospun scaffolds with tailored three-dimensional micro-patterns employing additive manufacturing. Biofabrication 6, 035003. https://doi.org/10.1088/1758-5082/6/3/035003

Ruspi, M.L., Palanca, M., Cristofolini, L., Liebsch, C., Villa, T., Brayda-Bruno, M., Galbusera, F., Wilke, H.-J., La Barbera, L., 2020. Digital Image Correlation (DIC) Assessment of the Non-Linear Response of the Anterior Longitudinal Ligament of the Spine during Flexion and Extension. Materials 13, 384. https://doi.org/10.3390/ma13020384

Sethuraman, V., Makornkaewkeyoon, K., Khalf, A., Madihally, S.V., 2013. Influence of scaffold forming techniques on stress relaxation behavior of polycaprolactone scaffolds. J. Appl. Polym. Sci. n/a-n/a. https://doi.org/10.1002/app.39599

Shah Hosseini, N., Simon, B., Messaoud, T., Khenoussi, N., Schacher, L., Adolphe, D., 2018. Quantitative approaches of nanofibers organization for biomedical patterned nanofibrous scaffold by image analysis: Quantitative approaches of nanofibers organization for biomedical patterned nanofibrous scaffold by image analysis. Journal of Biomedical Materials Research Part A 106, 2963–2972. https://doi.org/10.1002/jbm.a.36485

Shamsah, A., Cartmell, S., Richardson, S., Bosworth, L., 2019. Mimicking the Annulus Fibrosus Using Electrospun Polyester Blended Scaffolds. Nanomaterials 9, 537. https://doi.org/10.3390/nano9040537

Silberstein, M.N., Pai, C.-L., Rutledge, G.C., Boyce, M.C., 2012. Elastic–plastic behavior of non-woven fibrous mats. Journal of the Mechanics and Physics of Solids 60, 295–318. https://doi.org/10.1016/j.jmps.2011.10.007

Simonet, M., Stingelin, N., Wismans, J.G.F., Oomens, C.W.J., Driessen-Mol, A., Baaijens, F.P.T., 2014. Tailoring the void space and mechanical properties in electrospun scaffolds towards physiological ranges. J. Mater. Chem. B 2, 305–313. https://doi.org/10.1039/C3TB20995D

Sinha-Ray, S., Yarin, A.L., Pourdeyhimi, B., 2014. Meltblown fiber mats and their tensile strength. Polymer 55, 4241–4247. https://doi.org/10.1016/j.polymer.2014.05.025

Soliman, S., Sant, S., Nichol, J.W., Khabiry, M., Traversa, E., Khademhosseini, A., 2011. Controlling the porosity of fibrous scaffolds by modulating the fiber diameter and packing density. J. Biomed. Mater. Res. 96A, 566–574. https://doi.org/10.1002/jbm.a.33010

Tallawi, M., Dippold, D., Rai, R., D'Atri, D., Roether, J.A., Schubert, D.W., Rosellini, E., Engel, F.B., Boccaccini, A.R., 2016. Novel PGS/PCL electrospun fiber mats with patterned topographical features for cardiac patch applications. Materials Science and Engineering: C 69, 569–576. https://doi.org/10.1016/j.msec.2016.06.083

Titov, K., Tan, J.-C., 2016. Facile patterning of electrospun polymer fibers enabled by electrostatic lensing interactions. APL Materials 4, 086107. https://doi.org/10.1063/1.4960982

Vaquette, C., Cooper-White, J.J., 2011. Increasing electrospun scaffold pore size with tailored collectors for improved cell penetration. Acta Biomaterialia 7, 2544–2557. https://doi.org/10.1016/j.actbio.2011.02.036

Waheed, S., Butcher, A.L., Oyen, M.L., 2018. The viscoelastic response of electrospun poly(vinyl alcohol) mats. Journal of the Mechanical Behavior of Biomedical Materials 77, 383–388. https://doi.org/10.1016/j.jmbbm.2017.09.029

Wang, Y., Li, H., Wang, G., Yin, T., Wang, B., Yu, Q., 2010. Electrospinning of Polymer Nanofibers with Ordered Patterns and Architectures. Journal of Nanoscience and Nanotechnology 10, 1699–1706. https://doi.org/10.1166/jnn.2010.2149

Wang, Y., Wang, G., Chen, L., Li, H., Yin, T., Wang, B., Lee, J.C.-M., Yu, Q., 2009. Electrospun nanofiber meshes with tailored architectures and patterns as potential tissue-engineering scaffolds. Biofabrication 1. https://doi.org/10.1088/1758-5082/1/1/015001

Wittmer, C.R., Hébraud, A., Nedjari, S., Schlatter, G., 2014. Well-organized 3D nanofibrous composite constructs using cooperative effects between electrospinning and electrospraying. Polymer 55, 5781–5787. https://doi.org/10.1016/j.polymer.2014.08.044

Wu, H.-J., Hu, M.-H., Tuan-Mu, H.-Y., Hu, J.-J., 2019. Preparation of aligned poly(glycerol sebacate) fibrous membranes for anisotropic tissue engineering. Materials Science and Engineering: C 100, 30–37. https://doi.org/10.1016/j.msec.2019.02.098

Wu, Y., Dong, Z., Wilson, S., Clark, R.L., 2010. Template-assisted assembly of electrospun fibers. Polymer 51, 3244–3248. https://doi.org/10.1016/j.polymer.2010.04.039

Yan, D., Jones, J., Yuan, X., Xu, X., Sheng, J., C-M Lee, J., Ma, G., Yu, Q., 2013. Plasma treatment of random and aligned electrospun PCL nanofibers. Journal of Medical and Biological Engineering 33, 171–178. https://doi.org/10.5405/jmbe.1072

Yao, T., Chen, H., Samal, P., Giselbrecht, S., Baker, M.B., Moroni, L., 2019. Self-assembly of electrospun nanofibers into gradient honeycomb structures. Materials & Design 168, 107614. https://doi.org/10.1016/j.matdes.2019.107614

Yazhou Wang, Guixue Wang, Quingsong Yu, 2009. Electrospun nanofiber meshes with tailored architectures and patterns as potential tissue-engineering scaffolds. Biofabrication 2_3.

Zhang, D., Chang, J., 2007. Patterning of Electrospun Fibers Using Electroconductive Templates. Advanced Materials 19, 3664–3667. https://doi.org/10.1002/adma.200700896

Zhang, K., Wang, X., Jing, D., Yang, Y., Zhu, M., 2009. Bionic electrospun ultrafine fibrous poly(L-lactic acid) scaffolds with a multi-scale structure. Biomedical Materials 4, 035004. https://doi.org/10.1088/1748-6041/4/3/035004

Zhao, S., Zhou, Q., Long, Y.-Z., Sun, G.-H., Zhang, Y., 2013. Nanofibrous patterns by direct electrospinning of nanofibers onto topographically structured non-conductive substrates. Nanoscale 5, 4993. https://doi.org/10.1039/c3nr00676j

Zhou, Y., Tan, G.Z., 2017. Fabrication of nanofiber mats with microstructure gradient by cone electrospinning. Nanomaterials and Nanotechnology 7, 184798041774847. https://doi.org/10.1177/1847980417748478

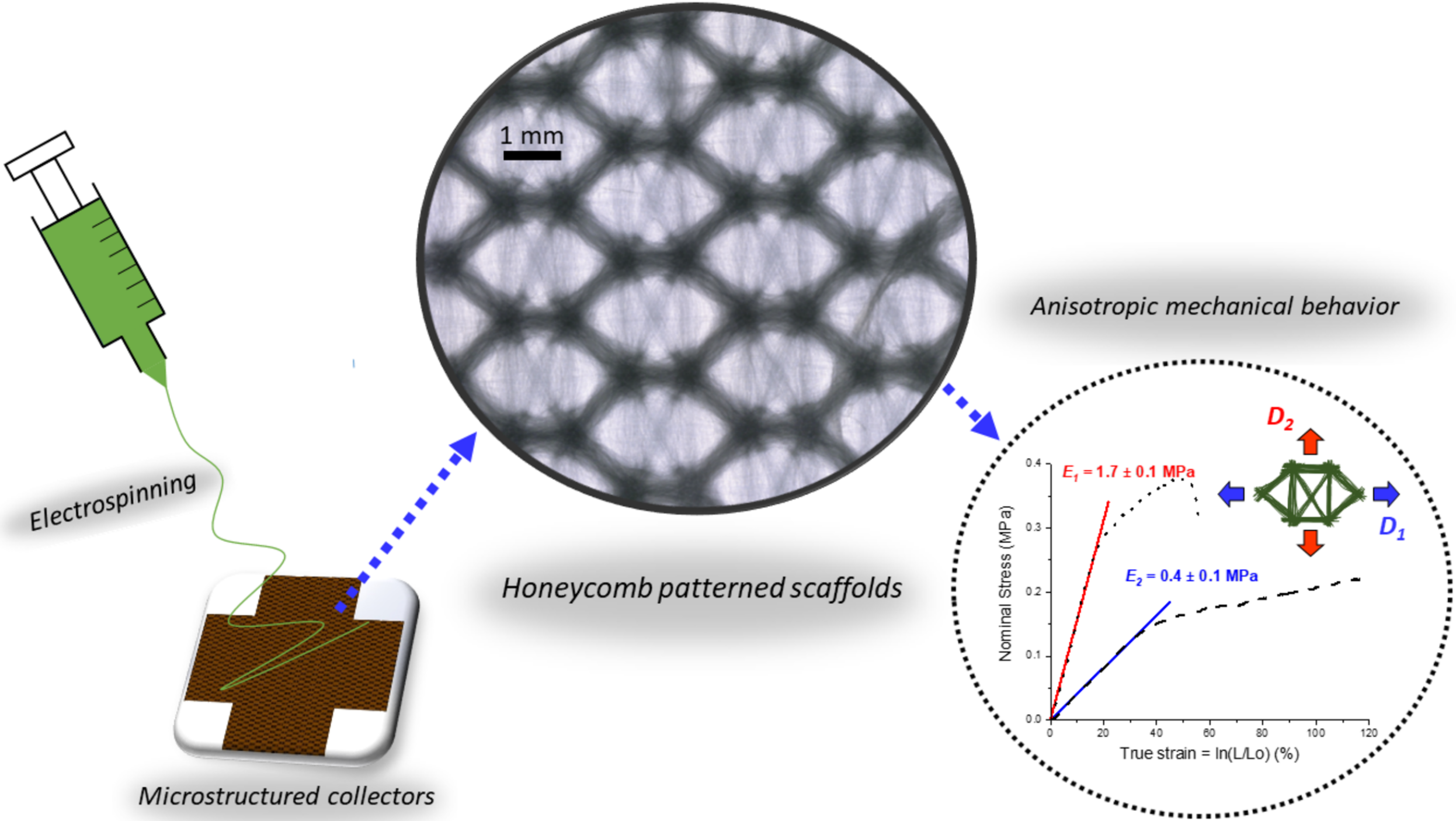
1 mm
Electrospinning
Microstructured collectors
Honeycomb patterned scaffolds
Anisotropic mechanical behavior
D2
D1
E1 = 1.7 ± 0.1 MPa
E2 = 0.4 ± 0.1 MPa
Nominal Stress (MPa)
True strain = ln(L/Lo) (%)
0.0
0.1
0.2
0.3
0.4
0
20
40
60
80
100
120